# A novel control method to maximize the energy-harvesting capability of an adjustable slope angle wave energy converter

**Nguyen Minh Tri[a], Dinh Quang Truong[b], Do Hoang Thinh[a], Phan Cong Binh[b], Dang Tri Dung[a], Seyoung Lee[a], Hyung Gyu Park[b], and Kyoung Kwan Ahn[b,*]**

[a]*Graduate School of Mechanical and Automotive Engineering of the University of Ulsan, Korea*

[b]*School of Mechanical Engineering, University of Ulsan, Ulsan, Korea*

[*]*Corresponding author: Tel.: +82-52-259-2282; fax: +82-52-259-1680*

*E-mail address: kkahn@ulsan.ac.kr*

**ABSTRACT**

This paper introduces a novel control approach to maximizing the output energy of an adjustable slope angle wave energy converter (ASAWEC) with oil-hydraulic power take-off. Different from typical floating-buoy WECs, the ASAWEC is capable of capturing wave energy from both heave and surge modes of wave motions. For different waves, online determination of the titling angle plays a significant role in optimizing the overall efficiency of the ASAWEC. To enhance this task, the proposed method was developed based on a learning vector quantitative neural network (LVQNN) algorithm. First, the LVQNN-based supervisor controller detects wave conditions and directly produces the optimal titling angles. Second, a so-called efficiency optimization mechanism (EOM) with a secondary controller was designed to regulate automatically the ASAWEC slope angle to the desired value sent from the supervisor controller. A prototype of the ASAWEC was fabricated and a series of simulations and experiments was performed to train the supervisor controller and validate the effectiveness of the proposed control approach with regular waves. The results indicated that the system could reach the optimal angle within 2s and subsequently, the output energy could be maximized. Compared to the performance of a system with a vertically fixed slope angle, an increase of 5% in the overall efficiency was achieved. In addition, simulations of the controlled system were performed with irregular waves to confirm the applicability of the proposed approach in practice.

***Key Words*:** Wave energy converter, ASAWEC, oil-hydraulic power take-off, learning vector quantitative neural network, control systems.

## 1. Introduction

Among various sources of renewable energy, ocean wave energy is important, as it has significant potential in many locations, due to its relatively high power density and predictability

[1]. Therefore, wave energy conversion technologies have gained more attention to meet the increasing demand for electrical power.

To harvest energy from waves, floating-buoy type wave energy converter (WEC) is the simplest and most popular design, and has been a focus of research. To maximize energy extraction from waves, the WEC must reach two optimal conditions, amplitude and phase, for each sinusoidal incident wave [2]. To satisfy the amplitude condition, the amplitudes of the radiated waves must be exactly half that of the incident waves [2,3]. To satisfy the phase condition, the oscillating velocity of the body must be in phase with the excitation force on the body. This can be achieved using phase control to obtain the resonance condition in which the wave frequency equals the natural frequency of the body. Here, two main control strategies, reactive control and latching control, are applied to WEC devices. Several interesting works have been reported [4-8]. Although phase control is capable of substantially increasing the amount of absorbed energy, implementation of this technique in real irregular waves has met both theoretical and practical difficulties that have not been satisfactorily overcome [9]. In addition, a phase control strategy requires governing equations for the body oscillations that are difficult to derive under real-world conditions. Modeling the highly non-linear behavior of both friction and wave characteristics is problematic.

To overcome the difficulty in regulating the power flow of WECs, neural networks (NNs) can be used to adaptively control the power-take-off (PTO) mechanisms [10]. As reported in [11,12], NNs were used to forecast the wave information in the near future to adjust in advance the PTO force. In another study [13], NN was utilized to derive the heuristic relationship between the system inputs and the control parameters. Although remarkable results were obtained using these approaches, the development and use of the control logic is complex, which restricts their applicability. Therefore, a simple and efficient way of maximizing WEC productivity without information on system dynamics is required.

To meet that requirement, this study focuses on a particular type of floating-buoy WEC, which was recently introduced: the adjustable slope angle wave energy converter (ASAWEC) [14]. The ASAWEC comprises mainly a sliding-buoy structure and a hydrostatic transmission-based PTO system. Different from typical floating-buoy designs, which are normally fixed vertically, an efficiency optimization mechanism (EOM) was integrated in the ASAWEC to enable adjustment of the system slope (or tilting angle) to increase the capture ratio from waves in both heave and surge modes. An analytical study of the interaction between waves and a buoy in the horizontal and vertical directions was carried out by Heikkinen et al. [15]. The results indicated that by combining the two modes to create the cylinder movement, the amount of absorbed energy could be increased. In the study by Thinh et al. [14], the effect of non-vertical linear motion of a

hemispherical-float wave energy converter was evaluated by both numerical simulations and experiments. The sliding angle exerted a significant impact on the energy capture ratio. Therefore, this paper aims to develop a simple control approach to maximize energy harvesting capability of the ASAWEC by regulating its slope angle. A control scheme that includes a supervisor controller and a secondary controller for the EOM mechanism is designed. The supervisor controller is constructed using a learning vector quantitative neural network (LVQNN) algorithm to classify wave conditions based on limited wave information, and so produces the optimal titling angles. The secondary controller with a simple control algorithm is used to drive the EOM mechanism to regulate automatically the ASAWEC slope angle to reach the value determined by the supervisor controller. In this way, the energy capture ratio is improved.

The remainder of this paper is organized as follows: in Section 2, the ASAWEC configuration is briefly introduced and, a mathematical model is developed for further investigation; in Section 3, a prototype of the suggested ASAWEC is fabricated and the experimental apparatus is discussed; the LVQNN-based on EOM control scheme is constructed and optimized using training data in Section 4; the proposed approach is evaluated by both numerical simulations and real-time experiments in Section 5; and concluding remarks are provided in Section 6.

## 2. EOM-Based ASAWEC design and modeling

### *2.1. EOM-based ASAWEC configuration*

To maximize the ability to harvest energy from waves, an ASAWEC device design is suggested in Fig. 1.

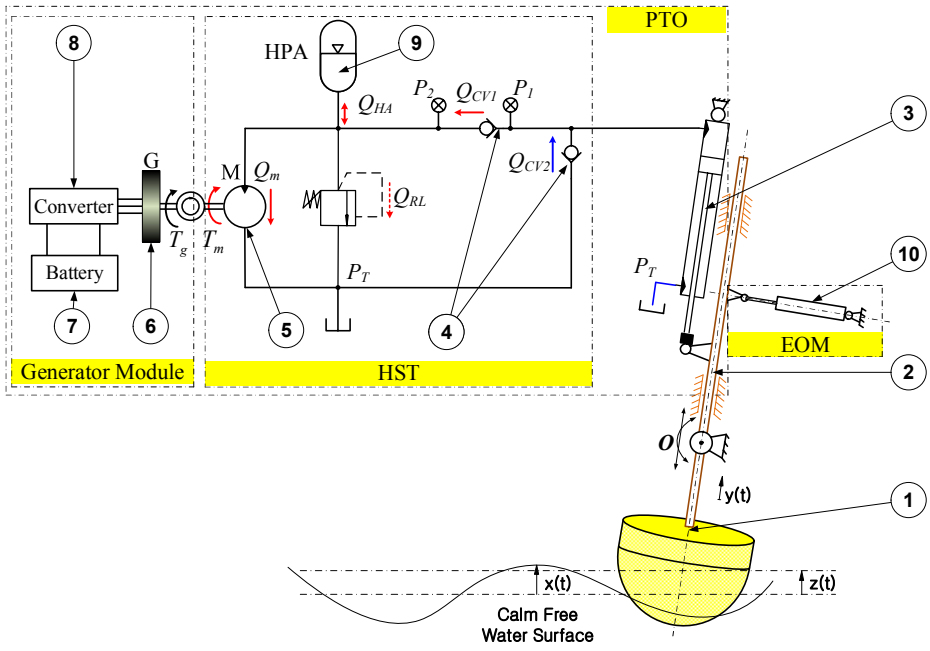


(1) Sub-buoy (2) Sliding shaft

(3) Hydraulic cylinder (4) Check valves
(5) One-directional hydraulic motor (6) Electric generator
(7) Battery (8) Converter
(9) High pressure accumulator (10) EOM

**Fig. 1** Configuration of the proposed ASAWEC

The ASAWEC includes the following two modules:

- PTO module: converts wave energy into electric energy. This consists of a hydrostatic transmission (HST) and an electrical generator. The system interacts with waves through a sub-buoy jointed with a sliding shaft. This shaft can slide along sliding bearings or through rollers fixed on the device frame. The sliding shaft is then linked in parallel to a non-symmetric hydraulic cylinder. To convert mechanical energy into hydraulic energy, the HST is a simple hydraulic circuit with a one-directional hydraulic motor, a high-pressure accumulator (HPA), check valves and a small oil sump. The mechanical energy of the PTO is transmitted to the HST through the large chamber of the cylinder, while the small chamber is connected to the oil sump. For safety, a pressure relief valve is used to protect the system from damage due to extremely high power waves. Next, a generator block is employed to generate electric energy from hydraulic energy. This block comprises an electrical generator, a converter and an electricity storage device, such as battery. The output shaft of the hydraulic motor is coupled to the generator shaft to generate electricity.
- EOM module: designed based on the ASAWEC configuration. A linear actuator with an appropriate driver is selected as the power source for the EOM. A controller is designed for this mechanism in order to adjust automatically the tilting angle of the PTO according to wave conditions in such a way that the device can absorb most of the energy from waves.

During operation, waves force the sub-buoy to move up and down based on the floating-buoy concept. Here, only upward motion of the sub-buoy is utilized for energy harvesting. During upward motion, the cylinder is retracted and a high-pressure flow is created in the large cylinder chamber. This pressurized flow enters the hydraulic circuit through the first check valve (CV1) and reaches the inlet of the hydraulic motor. Consequently, in this case the electric generator operates to generate electricity. In contrast, during downward motion of the cylinder, the low-pressure flow is supplied from the oil sump to fill the large cylinder chamber through the second check valve (CV2). The pressure at the hydraulic motor side is not affected in this case. To store redundant energy generated by large waves and to facilitate smooth performance of the electric generator between upward and downward motion of the sub-buoy, an HPA accumulator is employed. Using this HPA, the generator speed does not decrease to zero when the cylinder extends, and so, the system performance is improved.

## 2.2. Modeling of the ASAWEC device

### 2.2.1. Equations of motion

Generally, real ocean wave evaluation can be represented as [16]:

$$x = \sum_{n=-\infty}^{+\infty} Z_n \exp^{i2\pi nft}\, dt \tag{1}$$

where $Z_n = (1/T)\int_{-T/2}^{T/2} x(t) \exp^{-i2\pi nft}\, dt$, $(n = 0,1,2,...)$, $f = 2\pi / T$ is the fundamental frequency.

The mean wave power ($P_{wave}$) can be described as a function of the mean wave energy density and the group velocity [2]:

$$P_{wave} = E c_g \tag{2}$$

where $E$ is the mean wave energy density per horizontal unit area and is computed as:

$$E = E_k + E_p = \frac{1}{8}\rho g^2 H^2 \tag{3}$$

and $c_g$ is the group velocity. For a constant water depth $h$ at near shore locations (neither deep nor shallow water), the group velocity is obtained as follows:

$$c_g = \frac{D(kh)}{2\tanh(kh)} c_p = \frac{g}{2\omega} D\left(kh\right) \tag{4}$$

where $D\left(kh\right)$ is the depth function:

$$D\left(kh\right) = \left[1 + \frac{2kh}{\sinh(2kh)}\right] \tanh\left(kh\right) \tag{5}$$

here $k$ is the wave number and is determined as follows: $k = 2\pi / \lambda$.

An analysis of forces acting on the PTO mechanism is shown in Fig. 2. Assume that the PTO tilting angle is adjusted to angle $\alpha_{WEC}$ by the EOM. The movement of the sub-buoy as well as the cylinder rod is then on an incline axis tagged as $y(t)$. The buoy motion is then obtained following Newton's second law:

$$M\ddot{y} = F_{WEC} + F_u = F_W \cos\left(\alpha_{WEC} - \alpha_W\right) + F_u \tag{6}$$

where $M$ is the total mass of the moving parts, mainly the sub-buoy, sliding shaft and piston rod; $\alpha_W$ is the direction of the sum of hydrodynamic forces; $F_u$ is the force supported by a control device assisting the oscillating body operation; and $F_W$ is the sum of hydrodynamic forces acting on the cylinder rod.

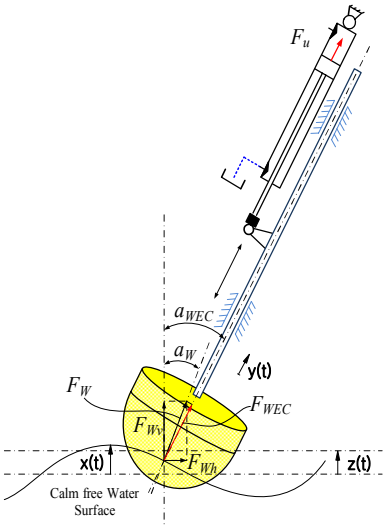


**Fig. 2** Analysis of forces acting on the PTO mechanism

The sum of hydrodynamic forces acting on the cylinder rod can be obtained by the following relation:

$$\vec{F}_W = \vec{F}_{Wv} + \vec{F}_{Wh} \tag{7}$$

where $\vec{F}_{Wv}$ and $\vec{F}_{Wh}$ are in turn the hydrodynamic forces in the vertical and horizontal directions.

In the vertical direction with heave motion [2], the hydrodynamic forces can be derived as:

$$F_{Wv} = F_{ev} + F_{rv} + F_b + F_v + F_f - Mg \tag{8}$$

where $F_{ev}$ is excitation force, $F_{rv}$ is the radiated force acting on the buoy in heave motion (vertical direction); $F_b$ is hydrostatic buoyancy force; $F_v$ is the viscosity effect and $F_f$ is the friction effect.

In the horizontal direction with drag motion [2], the hydrodynamic force is computed as:

$$F_{Wh} = F_{eh} + F_{rh} \tag{9}$$

where $F_{eh}$ is excitation force; $F_{rh}$ is the radiated force acting on the buoy in surge motion (horizontal direction).

The excitation force can be expressed as in equation (10):

$$F_w = \sqrt{F_{Wh}^2 + F_{Wv}^2} \tag{10}$$

*2.2.2. HST model*

From Fig. 2, the force $F_u$ can be derived as:

$$F_u = F_{PTO} + F_{mf} \tag{11}$$

where $F_{mf}$ is the total mechanical friction force existing in the system and $F_{PTO}$ is the force generated by the fluid in the cylinder:

$$F_{PTO} = P_1 A_{LC} - P_T A_{SC} \tag{12}$$

where $P_1/A_{LC}$ and $P_T/A_{SC}$ are the pressure/section area of the cylinder large and small chambers, respectively. These areas are obtained from the piston bore, $D_{cyl}$, and piston rod, $d_{cyl}$, as:

$$A_{LC} = \frac{\pi D_{cyl}^2}{4}; A_{SC} = \frac{\pi\left(D_{cyl}^2 - d_{cyl}^2\right)}{4} \tag{13}$$

In this system configuration, $P_T$ is neglected because the small cylinder chamber is connected to the tank. Then, the reactive force $F_{PTO}$ is generally determined from the characteristics of the HTS:

$$F_{PTO} = P_1 A_{LC} \tag{14}$$

where $P_1$ is the pressure inside the bore chamber:

$$\frac{dP_1}{dt} = \frac{\beta}{V_0 - A_{LC} z}\left(A_{LC}\dot{z} - Q_{cv1} + Q_{cv2}\right) \tag{15}$$

where $\beta$ is the bulk modulus of fluid; $L$ is the cylinder stroke, and $Q_{cv1}$ and $Q_{cv2}$ are the flow rates through check valve 1 and check valve 2, respectively. They are obtained using the following equations [17]:

$$\begin{cases} Q_{cv1} = C_d A_{o1}\sqrt{\dfrac{2(P_1 - P_2)}{\rho_f}} & if\ P_1 > P_2 \\ Q_{cv1} = 0, & if\ P_1 \le P_2 \end{cases} \tag{16}$$

$$\begin{cases} Q_{cv2} = C_d A_{o2}\sqrt{\dfrac{2(P_t - P_1)}{\rho_f}} & if\ P_t > P_1 \\ Q_{cv2} = 0, & if\ P_t \le P_1 \end{cases} \tag{17}$$

where $C_d$ is the discharge coefficient, $A_{o1}$ and $A_{o2}$ are the working area of each check valve, $\rho_f$ is the fluid density, $P_t$ is the pressure of the fluid inside the tank, and $P_2$ is the pressure in the chamber connected to the high-pressure accumulator and can be obtained by the continuity:

$$\frac{dP_2}{dt} = \frac{\beta}{V_p + V_{ha}}\left(Q_{cv1} - Q_{ha} - Q_m\right) \tag{18}$$

where $Q_m$ and $Q_{ha}$ are the flow rates through the hydraulic motor and into the HPA, respectively; $V_p$ is the volume of fluid inside the segment pipe that connects check valve 1 to the input port of the motor, and $V_{ha}$ is the fluid volume in the accumulator.

The flow rate $Q_{ha}$ and fluid volume $V_{ha}$, which enter the accumulator, are calculated as:

$$V_{ha} = \begin{cases} 0, & if\ P_2 \le P_0 \\ V_0\left[1-\left(\frac{p_0}{p_2}\right)^{\frac{1}{n}}\right], & if\ P_2 > P_0 \end{cases} \tag{19}$$

$$Q_{ha} = \dot{V}_{ha} = \begin{cases} 0, & if\ P_2 \le P_0 \\ \frac{1}{n}V_0\left(1-\frac{P_0}{P_2}\right)^{\frac{1-n}{n}}\frac{P_0\dot{P}_2}{P_2^2}, & if\ P_2 > P_0 \end{cases} \tag{20}$$

where $V_0$ is the accumulator capacity, $P_0$ is the pre-charge pressure, $P_2$ is the inlet gauge pressure of accumulator and $n$ is the specific heat ratio.

And the flow rate via the hydraulic motor is defined as:

$$Q_m = D_m\omega_m / \eta_v \tag{21}$$

where $D_m, \omega_m$ and $\eta_v$ are the displacement, angular speed and volumetric efficiency of the motor.

The actual output torque of the motor is given as:

$$\tau_m = \Delta p D_m \eta_m / 2\pi \tag{22}$$

where, $\Delta p$ is the pressure difference between two ports of the motor, and $\eta_m$ is the mechanical efficiency.

The electric power generated by the electric generator with overall efficiency $\eta_g$ can be evaluated as:

$$P_{generator} = \eta_g 2\pi\omega_g\tau_g = \eta_g 2\pi\omega_m\tau_m \tag{23}$$

where $\tau_g$ and $\omega_g$ are in turn the torque and angular speed of the electric generator.

*2.2.3. EOM force analysis*

To drive the shaft-buoy to the optimal angle, an EOM using a linear actuator is integrated into the ASAWEC (Fig. 1). To select this actuator, which is capable of raising or lowering the shaft-buoy mechanism irrespective of wave lifting force, a moment analysis around the fulcrum "O" is carried out for the actuator force and shaft-buoy gravity force (Fig. 3). The moment balance equation, therefore, can be derived as follows:

$$Mg\sin\alpha_{WEC}a = F_{LA}\sin\alpha_{EOM}b \tag{24}$$

where $F_{LA}$ is the desired force to rotate the shaft-buoy system, and *a* and *b* are instant distances from the buoy gravity mass center and linear actuator to the fulcrum "O" when the system is at angle $\alpha_{WEC}$.

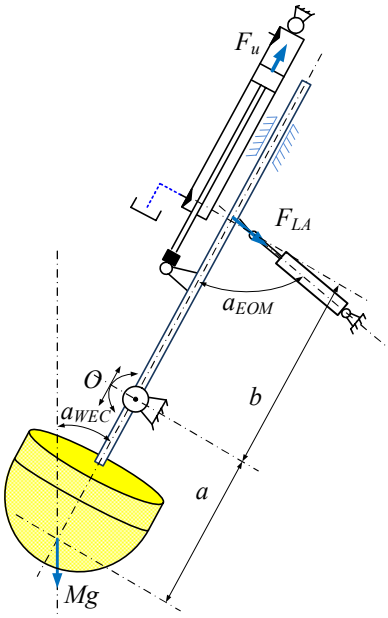


**Fig. 3** Detail view and force analysis of system

## 3. ASAWEC prototype and experimental setup

To investigate the performance of the proposed ASAWEC and the effect of the EOM mechanism on energy harvesting efficiency, a mini-scale ASAWEC prototype was produced.

### *3.1. ASAWEC component selection*

In the ASAWEC design, the buoy (Fig. 4) is of a composite material of which the outer and inner radiuses are $R_b$ and $r_b$, respectively. The buoy mass is calculated as:

$$m_b = \rho\left(V_s + V_c + V_{c1}\right) = \rho\left(\frac{2\pi}{3}\left(R_b^{\,3} - r_b^{\,3}\right) + \pi\left(R_b^{\,2} - r_b^{\,2}\right)h_b + \pi R_b^2\left(H_b - R_b - h_b\right)\right) \tag{25}$$

where $V_s, V_c$ and $V_{c1}$ are the volumes of the spherical part, cylindrical part and top cover, $\rho$ is the composite density, and $h_b$ and $H_b$ are in turn height of the cylinder part and total height of the buoy.

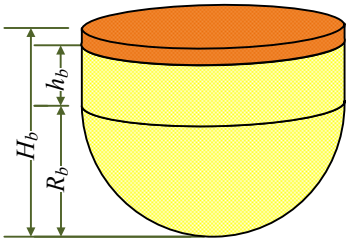


**Fig. 4** Buoy shape

Using buoy parameters of $R_b = 0.6m, r_b = 0.55m, H_b = 1m, h_b = 0.37m$ and $\rho = 800kg/m^3$, the mass of buoy is approximated as $m_b = 200kg$

Here, a magneto-rheological brake (MR Brake) of which the load torque, $\tau_{MR}$, is adjustable from 0 to 5.6*Nm* is used to represent the electric generator. Based on the model developed in the previous section, the key components for the system are as follows:

From Eq. (22), the motor displacement is:

$$D_m \geq \frac{2\pi \times \tau_m}{\Delta p \times \eta_m} = \frac{2\pi \times \tau_{MR\max}}{\Delta p \times \eta_m} \approx 11.16cm^3/rev \quad (26)$$

where, the motor mechanical efficiency and maximum working pressure are $\eta_m = 0.9$ and $\Delta p = 35bar$.

The maximum motor speed should be equal or greater to the maximum MR Brake speed ( $n_{MR\max} = 1000rpm$ ). Therefore, a fixed displacement gear motor with OML12.5 series manufactured by Danfoss with the following characteristics is selected:

$D_m = 12.5cm^3/rev, n_{m\max} = 1280rpm, T_{\max} = 11Nm, \ \eta_m = \eta_v = 0.85$.

The flow rate required to supply the motor for the maximum generator speed is then obtained:

$$Q_{m\max} \geq \frac{D_m n_{MR\max}}{\eta_v} \approx 14.71lpm \quad (27)$$

Here, the mini-scale ASAWEC is designed for evaluation with single waves of frequency of up to 1.5 Hz. Thus, based on the required flow rate, a cylinder with the following parameters is used: $D = 0.025m, d = 0.012m, L = 0.5m$.

Next, the linear actuator is selected based on the power on demand. From (24), the force $F_{LA}$ that must be supplied by this actuator can be calculated as:

$$F_{LA} = \frac{F_G \sin\alpha_{WEC} a}{\sin\alpha_{POM} b} \quad (28)$$

Practical testing on the ASAWEC indicates that, the tilting angle should be limited to 0 to 20°. Initial values of the distances *a* and *b* corresponding to the initial tilting angle (0°) are 1500 and 390 *mm*. The electric linear actuator made by Zhejiang Corp. with the following characteristics is used: 0.8*kW* power, 300*mm* stroke, and 7000*N* load capacity.

The specifications of the main components of the proposed system are summarized in Table A1 in the Appendix.

### *3.2. Experimental apparatus*

Using the components outlined in the previous section, the scaled ASAWEC system with the configuration shown in Fig. 2 was fabricated. A photograph of the system is shown in Fig. 5. To acquire the necessary information for system management and evaluation, sensors were attached to the system. The sub-buoy motion ($y$) was detected by a cable sensor, while the working pressures ($P_1$ and $P_2$) and flow rate ($Q_m$) of the HST were measured by two pressure transducers and a flow meter. To assess the output energy capable of generating electricity, a torque transducer integrated with a speed sensor was used to obtain the generated torque and speed of the MR brake ($T_g$ and $n_g$, respectively). Furthermore, another cable sensor was installed along the linear actuator to monitor indirectly the tilting angle of the sliding-buoy system. A personal computer (PC) was used to receive signals fed-back from the sensors and derive outputs to control the ASAWEC via an NI multi-function card. Software was developed within the Matlab/Simulink environment combined with the Real-time Windows Target toolbox to facilitate this task.

To investigate the performance of the EOM-based ASAWEC, a water tank integrated with a wave maker was created (Fig. 6). The specifications of the water tank and wave maker are shown in Table A2 in the Appendix.

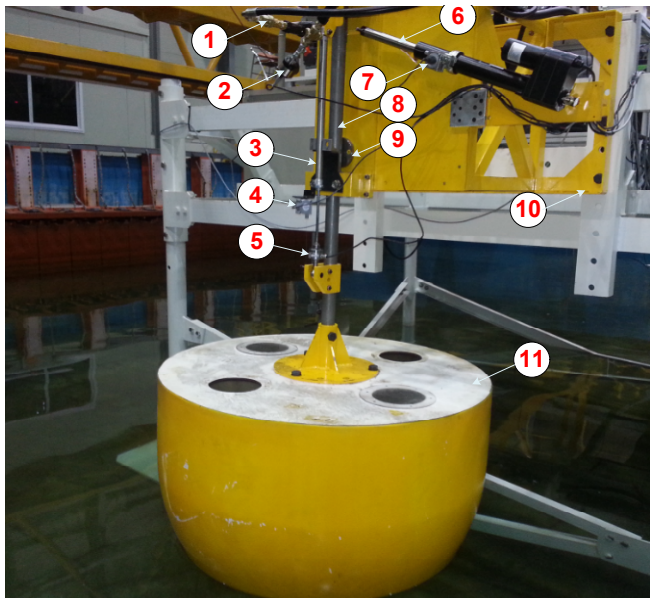


(a) PTO & EOM (1-Check Valve; 2-Pressure sensor 1; 3-Hydraulic cylinder; 4-Cable sensor 1; 5-Load cell; 6-Linear actuator; 7-Cable sensor 2; 8-Stell shaft; 9-Fulcrum “O”; 10-Base frame; 11-Sub-buoy)

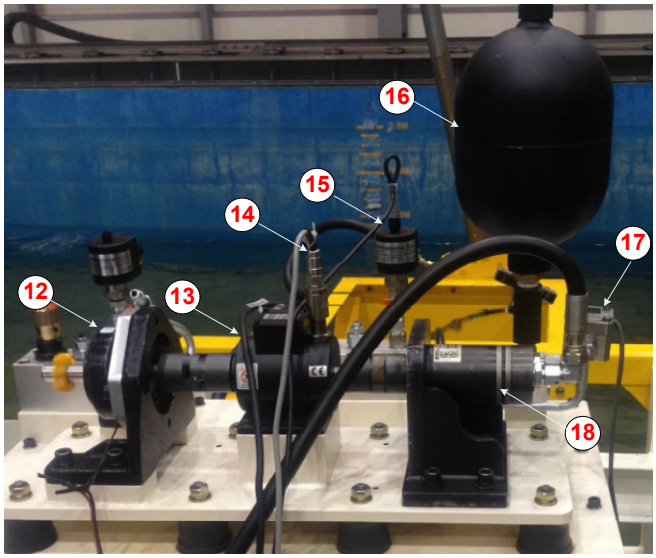


(b) HTS & MR brake (12-MR brake; 13-Torque transducer; 14-Speed sensor; 15-Pressure sensor 2; 16-HP accumulator; 17-Flow meter; 18-Pump)

**Fig. 5** Graphical view of the experimental EOM-based ASAWEC

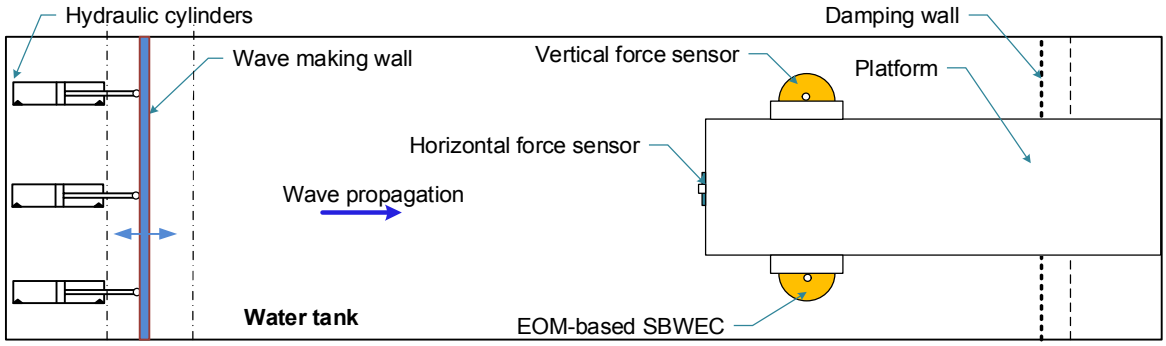


**Fig. 6** System installation in water tank integrated wave maker

## 4. EOM controller design

### *4.1. EOM overall control concept and secondary controller*

In this section, a controller is designed to drive the EOM to optimize the buoy-shaft tilting angle according to wave conditions. The control system configuration is depicted in Fig. 7. The controller consists of two sub-controllers: a supervisor controller and a secondary controller. The supervisor controller is designed using the LVQNN technique to detect each wave condition based on the wave information, tagged as $\eta_{Wave}$, and then, to derive the optimal tilting angle (or desired angle) for the ASAWEC, tagged as $\alpha_r$. The secondary controller uses a simple proportional-integral (PI) algorithm to drive the EOM to change the sliding-buoy mechanism to follow the desired angle. As a result, the maximum amount of wave energy can be absorbed.

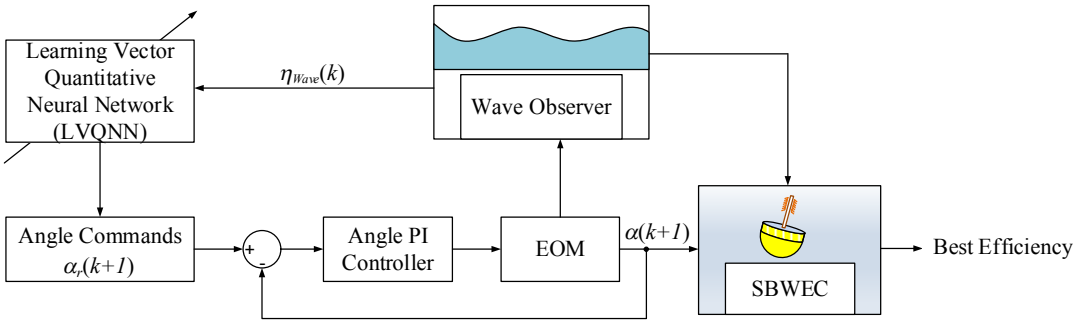


**Fig. 7** EOM control architecture for maximizing energy performance of ASAWEC

The PI controller was designed based on the model-based PID tuning function of MATLAB. Using the system identification toolbox of MATLAB, the EOM model was derived based on the input and output data of the linear actuator (driving voltage command and cylinder displacement, respectively) installed in the ASAWEC. Next, the resultant EOM model was combined with the ASAWEC model to tune the PI controller. As a result, the PI proportional and derivative gains, were achieved in turn as: $k_p = 0.8$ and $k_i = 0.01$.

### *4.2. LVQNN-based supervisory control*

#### *4.2.1. Learning vector quantitative neural network*

Neural networks (NNs) emulate the activity of biological neural networks. They can learn from a set of data and construct weight matrices to represent the learning patterns. This technique modifies its behavior in response to the environment and is ideal for unknown expected mapping algorithms and when tolerance to faulty input information is required. NNs have been used successfully for applications such as pattern classification, decision making, forecasting, and adaptive control [18].

Generally, NNs can be classified according to the learning process: supervised and unsupervised learning. Supervised learning is training using the desired responses to given stimuli, while unsupervised learning is classification by "clustering" of stimuli, without specified responses. LVQNN is a hybrid network that uses advanced behaviors of both competitive learning and applies a Kohonen self-organizing map (SOM) or Kohonen feature map for classification.

Fig. 8 shows the structure of a LVQNN. This LVQNN contains four layers: one input layer with $m$ nodes, two hidden layers, and one output layer with n nodes. The first hidden layer is termed the competitive layer with S1 nodes, while the second output layer is termed the linear layer with S2 nodes, (in this case, $S_2 \equiv n$).

During operation, the competitive layer first maps input vectors into the clusters found by the network through a training process. Secondly, the linear layer merges groups of these clusters into classes defined by the target data. The total number of clusters in the competitive layer is determined by the number of hidden neurons. The larger the hidden layer, the more clusters the competitive layer can learn, and the more complex mapping of input to target classes can be performed [19,20]. Therefore, with appropriate selection of the structure and training of the weighting factors, the LVQNN can classify the information of any system.

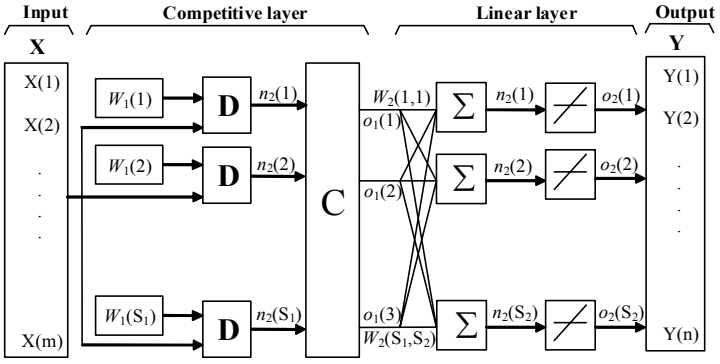


**Fig. 8** Structure of the LVQNN

The LVQNN is based on the nearest-neighbor method by calculating the Euclidean distance weight function, $D$, for each node, $n_j$, in the competitive layer as follows:

$$n_j = D\left(X, W_1(j)\right) = \sqrt{\sum_{i=1}^{m}\left(X(i) - W_1(j,i)\right)^2}, \quad j = 1,..,S_1 \tag{29}$$

where: $X$ is the input vector and $W_1(j,i)$ is the weight of node $j^{\text{th}}$ in the competitive layer corresponding to element $i^{\text{th}}$ of the input vector.

Next, the Euclidean distances are fed into function C which is a competitive transfer function. This function returns an output vector $o_1$, with 1 if each net input vector has its maximum value, and 0 otherwise. This vector is then input to the linear layer and derives the output vector $o_2$ of each element of which corresponds to a node of the output layer and is computed as:

$$Y(k) = o_2(k) = k_W(k)\, n_2(k) = k_W(k) \sum_{j=1}^{S_1} W_2(k,j)\, o_1(j), \quad k = 1,..,n, \left(n \equiv S_2\right) \tag{30}$$

where: $W_2(k,j)$ is the weight of node $k$ in the linear layer corresponding to element $j$ of the competitive output vector; and $k_W(k)$ is the linearized gain of node $k$ in the linear layer.

In the learning process, the weights of LVQNN are updated by the well-known Kohonen rule, which is shown as the following equation:

$$\begin{cases} W_1^{t+1}(j) = W_1^t(j) + \mu\left(X - W_1^t(j)\right) \text{ IF: } X \text{ is classified correctly} \\ W_1^{t+1}(j) = W_1^t(j) - \mu\left(X - W_1^t(j)\right) \text{ IF: } X \text{ is classified incorrectly} \end{cases}, j = 1,..,S_1 \tag{31}$$

where $\mu$ is the learning ratio with positive and decreased with respect to the number of training iterations ($n_{iteration}$), $\mu = \frac{1}{n_{iteration}}$

*4.2.2. Application of LVQNN to a supervisor controller design*

In this study, the LVQNN was employed to design the supervisor controller to distinguish different wave conditions in an online manner. In LVQNN, it is important to determine the input vector size and the number of data sequences. In general, a better result can be achieved with more inputs. However, this makes the network complex and difficult to train. For application to a specific water region, the ASAWEC was installed in such a way that its tilting plane was mostly parallel to the propagation direction of the wave components that contained the highest power density. Therefore, without loss of generality, to enhance the given task, three signals extracted from the feedback wave information, $\eta_{Wave}$ —wave fluctuation, hydrodynamic forces in the vertical direction $F_{Wv}$ and horizontal direction $F_{Wh}$— were used to create the input vector for the LVQNN, while the output was a specific wave case used to determine the desired angle (Fig. 9a). To acquire this information, a cable sensor and two load cells were installed, in which the axis of load cell measurement of the horizontal force was parallel to the ASAWEC tilting plan (Fig. 9b). It should be noted that these sensors were not attached to the ASAWEC, being located near the device because the sensed wave information should not be influenced by the change in system slope angle. Furthermore, the supervisor controller required only the relative wave behavior to classify wave conditions, information on transient wave impacts on the system was not required.

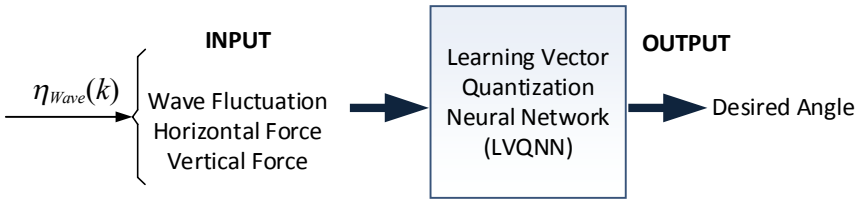


(a)

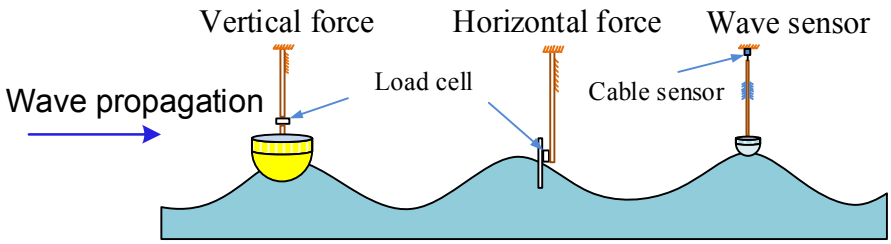


(b)

**Fig. 9** LVQNN-based supervisor controller:
(a) Control configuration; (b) Hardware setup to observe wave information

To classify ocean waves that contain many different frequencies, the output from the supervisor controller should be a wave condition (called a class), which is mixed from different waves by different mixing ratios. To facilitate this, a so-called smooth switching algorithm was proposed. The wave class was determined by the smooth combination of the current class detected by the LVQNN ($Y$) and the previous class as:

$$class(t) = \lambda \times class(t-1) + (1-\lambda) \times Y(t) \tag{32}$$

where $\lambda$ is the forgetting factor.

Similarly, the desired tilting angle is produced by:

$$\alpha_r(t) = \lambda \times \alpha_r|_{class(t-1)} + (1-\lambda) \times \alpha_r|_{Y(t)} \tag{33}$$

Additionally, to prevent the influence of noise on classification performance, the forgetting factor was online tuned with respect to the change in the LVQNN output speed. This factor was tuned as follows:

Step 1: set the initial value of the forgetting factor, $\lambda = 0.5$; define a small positive threshold, $0 < \gamma_1 < \gamma_2$, for the change in LVQNN output speed, $v_Y$, which is defined by the number of sampling periods during which $Y$ changes continuously.

Step 2: for each working step, check $v_Y$ and update $\lambda$ by comparing $v_Y$ with $\gamma$ using the following rule:

+ If: $v_Y = 0$, Then: $\lambda(t+1) = \lambda(t)$;

+ Else If: $(v_Y > \gamma_2)$, Then: $\lambda(t+1) = \lambda(t+1)/2$ and reset $v_Y = 0$;

+ Else If: $(v_Y \geq \gamma_1) \& (v_Y(t) \leq \gamma_2)$, Then: $\lambda(t+1) = \lambda(t+1) \times 2$ and reset $v_Y = 0$;

+ Otherwise, $\lambda(t+1) = \lambda(t)$.

In summary, the procedure to design the supervisor controller for application to real waves is as follows:

- Step 1: Observe of ocean waves at the location at which the ASAWEC system will be installed.
- Step 2: Analyze the observed waves to identify the major frequencies (for example, a set of seasonal main frequencies)
- Step 3: Train the LVQNN using the selected main frequencies (a set of LVQNN classifiers can be derived for a set of seasonal main frequencies and a real-time clock can be used to switch between these classifiers according to season)
- Step 4: Input the optimized LQVNN into the supervisor controller to regulate the ASAWEC slope.

### *4.3. Training of the supervisor controller*

#### *4.3.1. Acquisition of data for system performance investigation and training*

In a network-training problem, the prior task is to collect the system behavior data to improve the performance of the training process. To perform the investigation, single frequency waves whose specifications were shown in Table 1 were selected. Experiments on the ASAWEC were then carried out for each wave condition in which the tilting angle was altered smoothly within its range, 0 to 20$^{o}$, using the designed secondary controller (PI). For these experiments, the ASAWEC setting parameters were identical and the overall efficiency of the full system was evaluated. As described in the previous section, the wave factors necessary for performing the LVQNN input vector were recorded for each test case and plotted in Fig. 10. Both the wave elevation and forces were differed and therefore, could be used for wave classification.

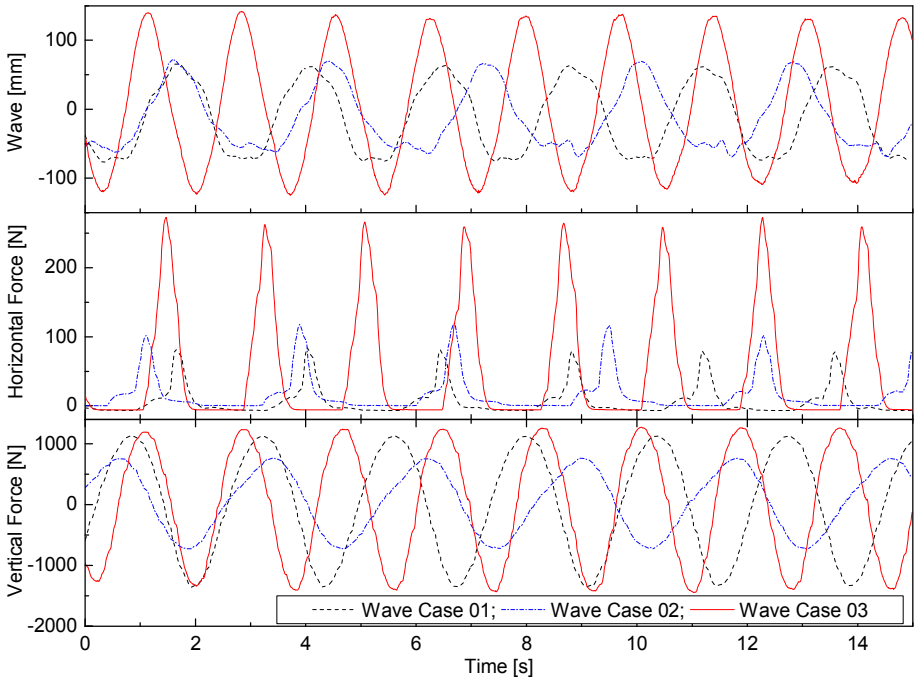


**Fig. 10** Data acquisition of three wave factors according to three test cases

**Table 1**

Wave specifications and optimal tilting angles

| Wave case | Wave specifications | | Optimal tilting angle [degree] |
|---|---|---|---|
| | Amplitude [m] | Period [s] | |
| 1 | 0.12 | 2.4 | 6.0 |
| 2 | 0.15 | 2.8 | 10.0 |
| 3 | 0.1 | 1.6 | 12.0 |

According to [21], the energy flux over duration $T$ for the shallow water in the water tank can be calculated as:

$$E_{inTank} = \frac{\rho g^{3/2} H^2 \sqrt{h} T b}{8} \tag{34}$$

Since, the average energy conversion efficiency of the system is derived as:

$$\eta_{ASAWEC} = \frac{\int_0^T P_{genereator}}{E_{inTank}} \tag{35}$$

The average efficiency curve of the system versus the tilting angle is shown in Fig. 11. It is clear that the efficiency differed according to the test case and tilting angle. The angles at which system efficiency was maximized for the three wave forms were determined (Table 1). In wave case 3, the greatest increase in overall efficiency of 5% was achieved compared to the case in which the sliding shaft was fixed in the vertical direction (zero degree, no change in the tilting angle).

Therefore, the supervisor controller was designed to drive the system to the optimal working point.

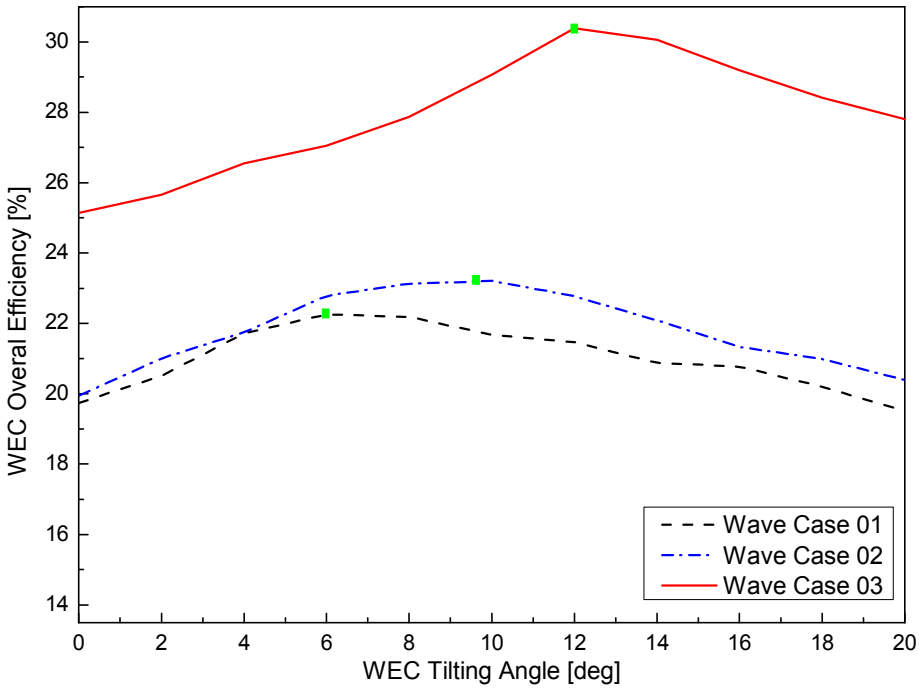


**Fig. 11** ASAWEC efficiency vs. tilting angle

*4.3.2. LVQNN training*

In this section, the training of the LVQNN is discussed. The data acquired in Section 4.3.1 were used as the input-output vectors. The wave information and optimal tilting angles data of the three test cases (Table 1) were selected for training the LVQNN.

As mentioned before, determination of a suitable input vector size and number of hidden neurons in the competitive layer is critical for practical implementation of the neural classifier. Here, the input vector size was defined based on the numbers of sequences of the three wave signals (the hydrodynamic forces in the vertical and horizontal directions, the wave frequencies). To investigate the performance of the LVQNN with respect to different structures, training was performed using the selected data set by varying the number of inputs from 6 to 18, and the number of hidden neurons from 20 to 50. After each training process, the correlation between the simulation output and target output was taken as indicative of the success of training. The training results (goodness of fit [%]) of the LVQNN are shown in Fig. 12 and Table 2. These results indicate that the most suitable LVQNN structure comprised 12 nodes in the input vector and 40 nodes in the competitive layer. The highest learning success rate was ~86.84% in that case, which was sufficient for recognition of wave conditions.

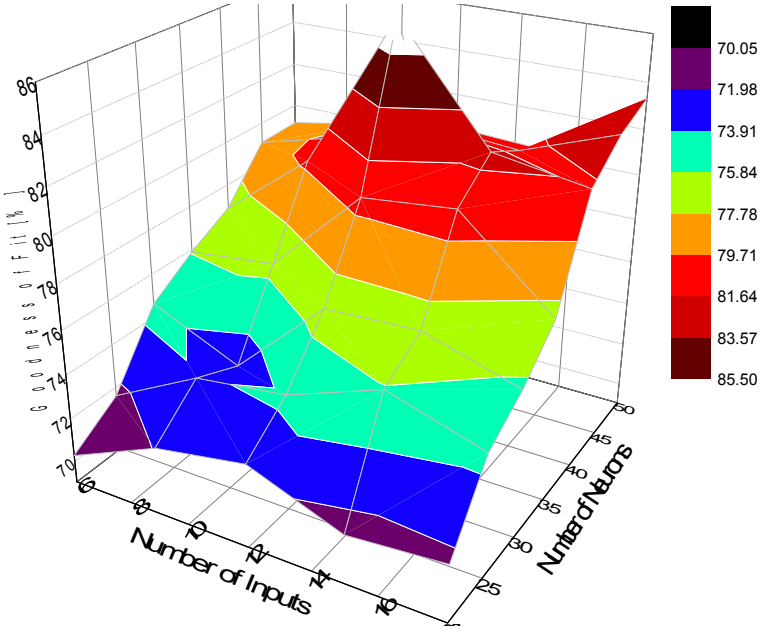


**Fig. 12** Goodness of fit – 3D map

**Table 2**

Learning success rate of LVQNN [%]

| Input Number | Number of nodes in hidden layer | | | | | | |
|---|---|---|---|---|---|---|---|
| | 20 | 25 | 30 | 35 | 40 | 45 | 50 |
| 6 | 70.27 | 71.59 | 74.62 | 75.88 | 76.91 | 79.08 | 79.15 |

| | | | | | | | |
|---|---|---|---|---|---|---|---|
| 9 | 72.04 | 73.71 | 72.84 | 76.35 | 79.98 | 80.13 | 79.85 |
| 12 | 72.76 | 74.23 | 76.64 | 80.28 | **86.84** | 81.53 | 80.47 |
| 15 | 71.19 | 75.77 | 76.83 | 80.73 | 82.06 | 81.19 | 80.26 |
| 18 | 71.56 | 74.49 | 75.58 | 77.17 | 81.43 | 82.69 | 83.31 |
| | Goodness of fit [%] | | | | | | |

## 5. Supervisor control verification

In this section, the capability of the supervisor controller was evaluated using both single frequency waves and irregular waves. From the results obtained in the previous section, the controller was constructed using the LVQNN with the optimal structure.

First, verification using single frequency waves by means of numerical simulations and real-time experiments is discussed. For the simulations, the three data sets (corresponding to the three cases in Table 3) were employed in turn. Then the classifier was operated to detect the wave conditions and the optimal tilting angles. Classification performance is shown in Figures 13 to 15 and compared with the target angles shown in Table 3. These results indicate that the classifier could detect the wave conditions and the output reach stably to the optimal angle in a short time; e.g., $6^{o}$ output after ~1.3 s for wave case 1. In test case 2, the optimized controller detected the wave condition and the desired tilting angle within 1 s. In test case 3, the time required by the controller to make a decision on the wave condition was longer (~2.7 s), because the number of wave factors used as controller inputs was limited to 3, and these had similar forms among the various wave cases.

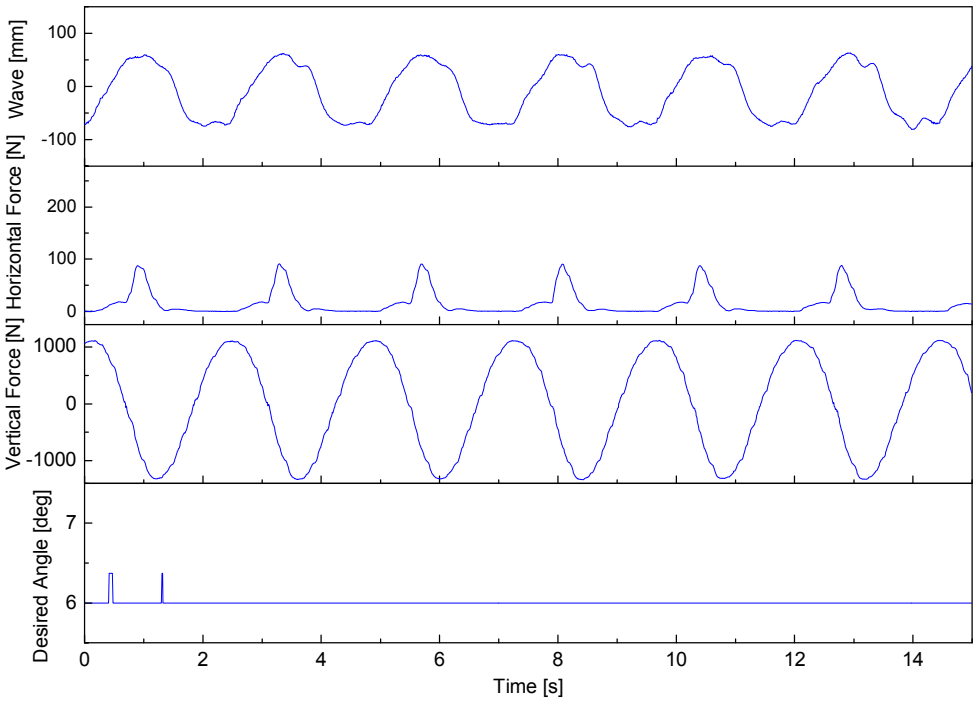


**Fig. 13** Simulation verification of the optimized LVQNN with respect to test case 1

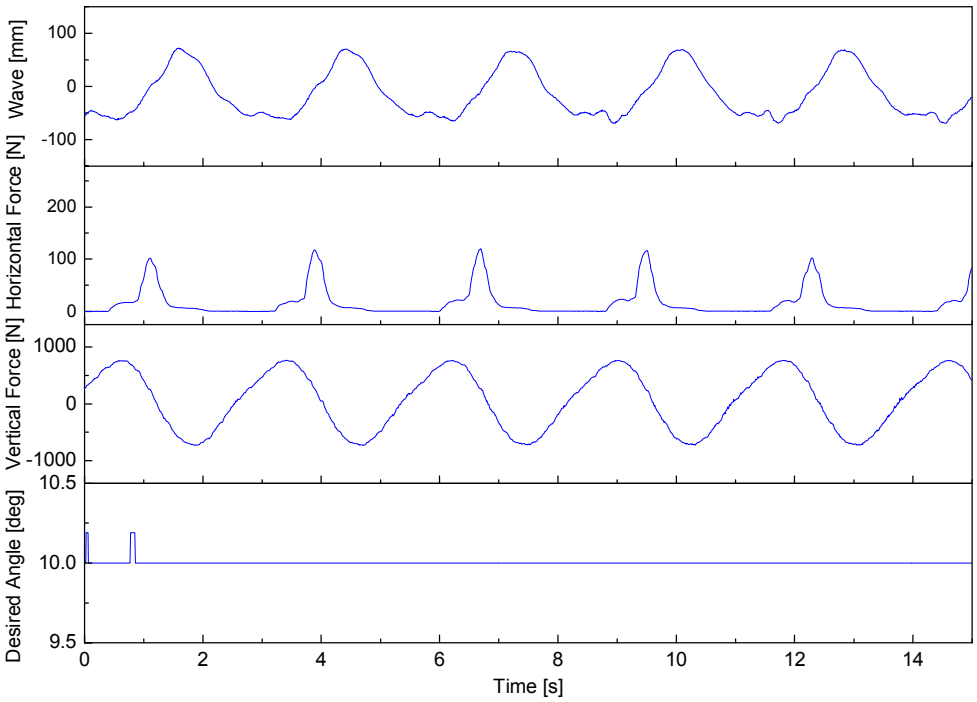


**Fig. 14** Simulation verification of the optimized LVQNN with respect to test case 2

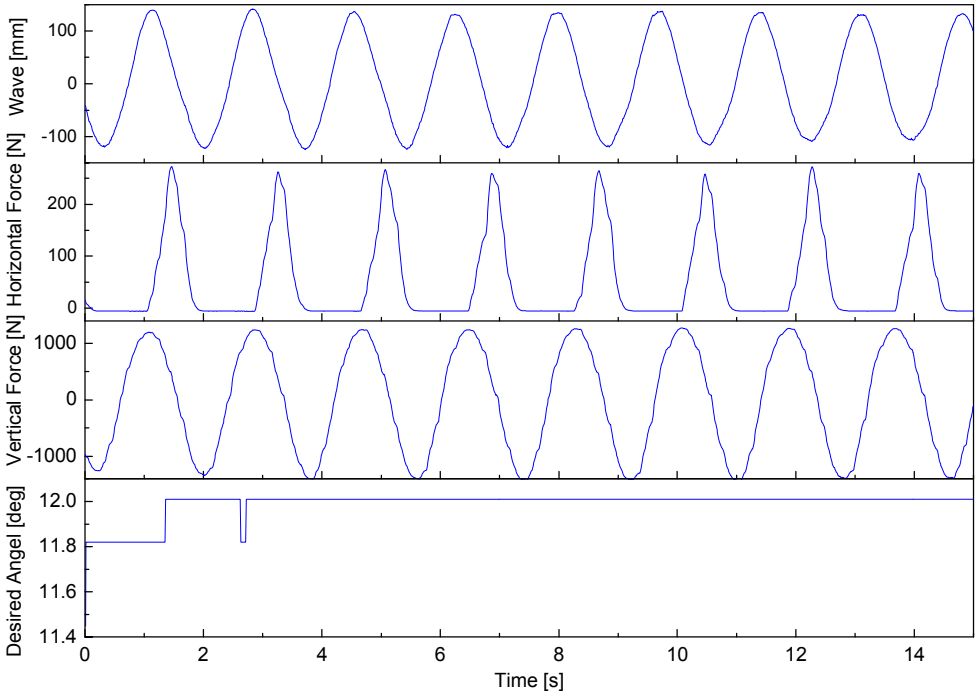


**Fig. 15** Simulation verification of the optimized LVQNN with respect to test case 3

Next, the real-time ability of the supervisor controller was investigated. The system was subjected to each of the three test cases in real-time. The wave classification and angle detection results are shown in Figures 16 to 18. The real-time wave detection performance was similar to the simulation performance. These results imply that the proposed classifier could detect the wave conditions. Therefore, it made precise decisions of tilting angles to maximize the energy harvesting capability of the device.

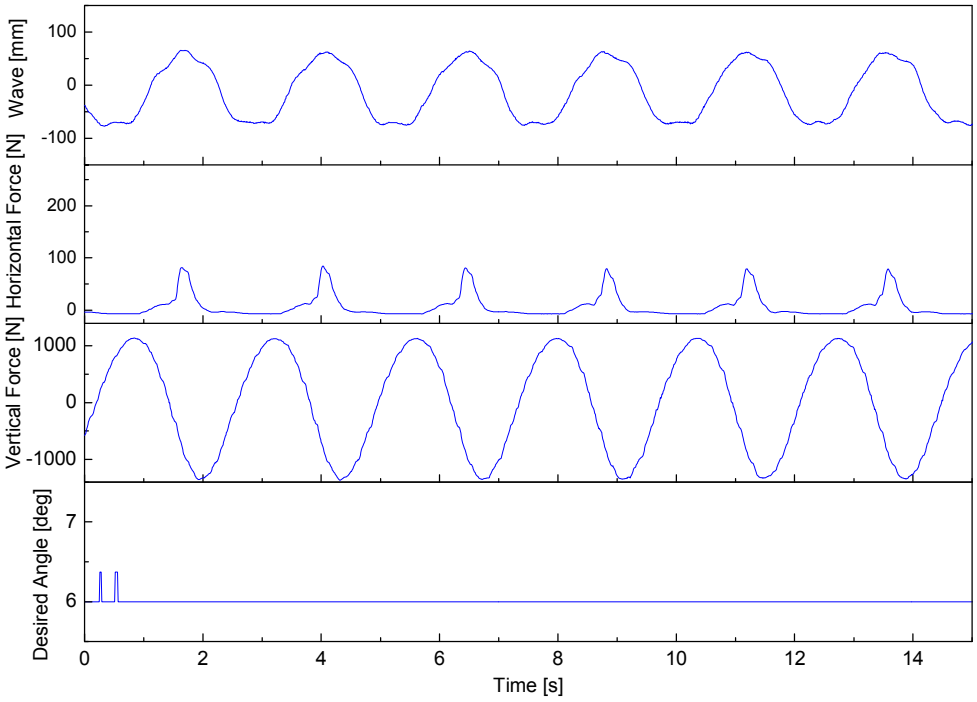


**Fig. 16** Experimental verification of the optimized control LVQNN with respect to test case 1

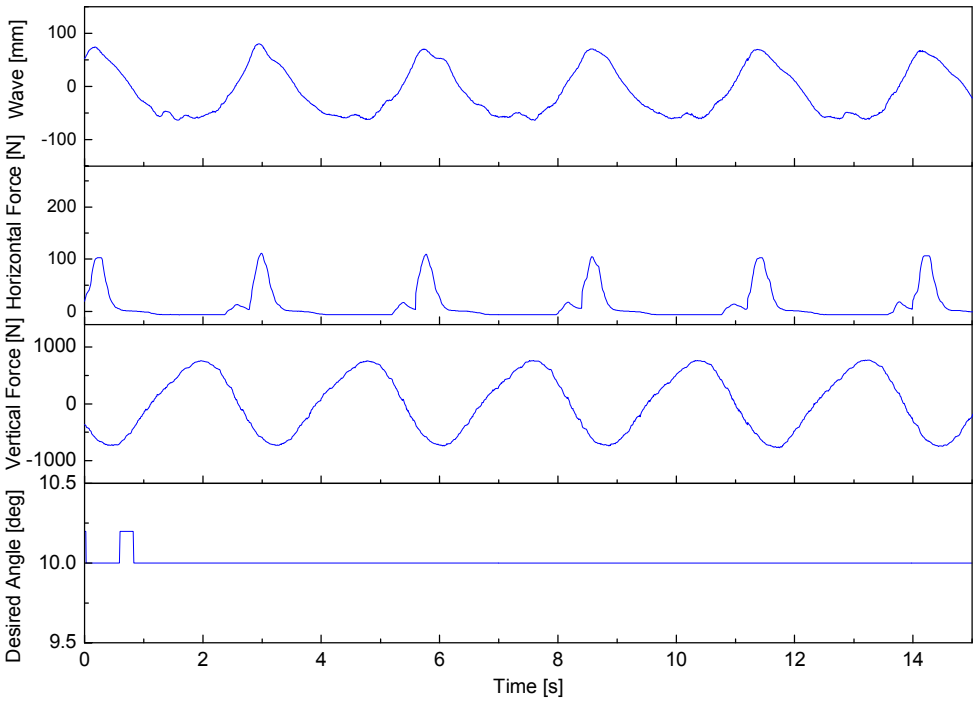


**Fig. 17** Experimental verification of the optimized control LVQNN with respect to test case 2

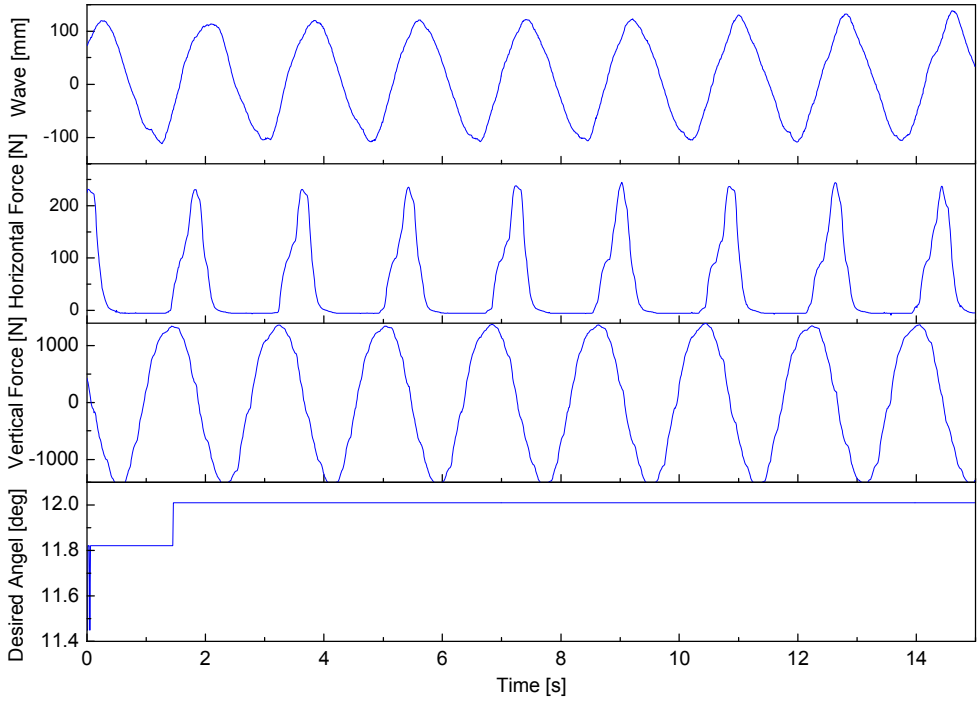


**Fig. 18** Experimental verification of the optimized LVQNN with respect to test case 3

Second, simulations were carried out for irregular waves to demonstrate the applicability of the proposed controller for real waves. Herein, irregular waves were simulated using the Pierson-Moskowitz spectrum formulation [2, 16]. To utilize the results in Section 4 in which the LVQNN was optimized for the wave cases in Table 1, a peak period of 2 s ($T_p$ = 2s), a significant wave height of 270 mm ($H$ = 270 mm), and a frequency range of 0.25-0.75 Hz were selected to generate the Pierson-Moskowitz wave spectra. Thus, the irregular waves covered the three wave cases in

Table 1; therefore, the procedure to derive the supervisor controller (as mentioned in Section 4.2.2) was employed. Simulations using the ASAWEC model developed in Section 2 were then performed with irregular waves for two cases: using the supervisor controller to regulate the slope angle, and with the slope fixed at an appropriate angle. The simulation with the supervisor controller was performed first (Fig. 19). The system slope was smoothly varied according to the wave variation. Subsequently, the simulated system efficiency was obtained (solid blue line in the top sub-plot of Fig. 20). Using the mean value of the desired angle regulation in Fig. 19, the second ASAWEC simulation was performed in which the slope angle was fixed at 7°. The simulated system efficiency was achieved (dash-dot black line in the top sub-plot of Fig. 20). The difference in efficiency due to use of the supervisor controller is depicted in the bottom sub-plot of Fig. 20. A maximum improvement in system efficiency of 2.8% was recorded in the irregular wave condition. These results demonstrate that system performance could be improved using the proposed control methodology.

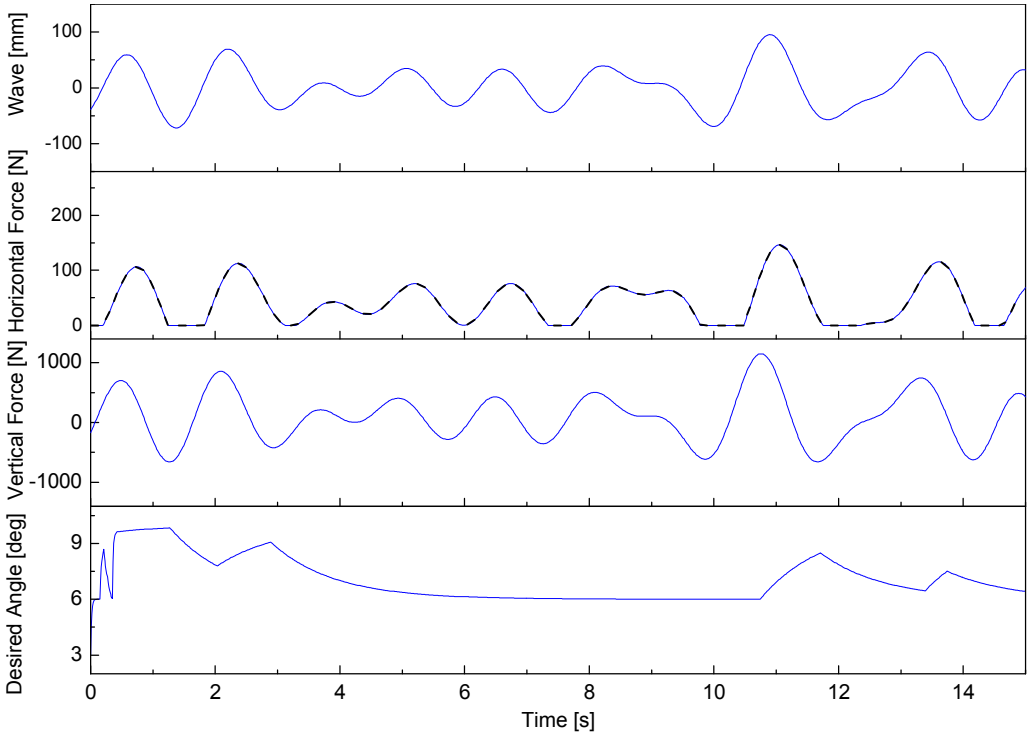


**Fig. 19** Simulation LVQNN classification result in irregular wave condition

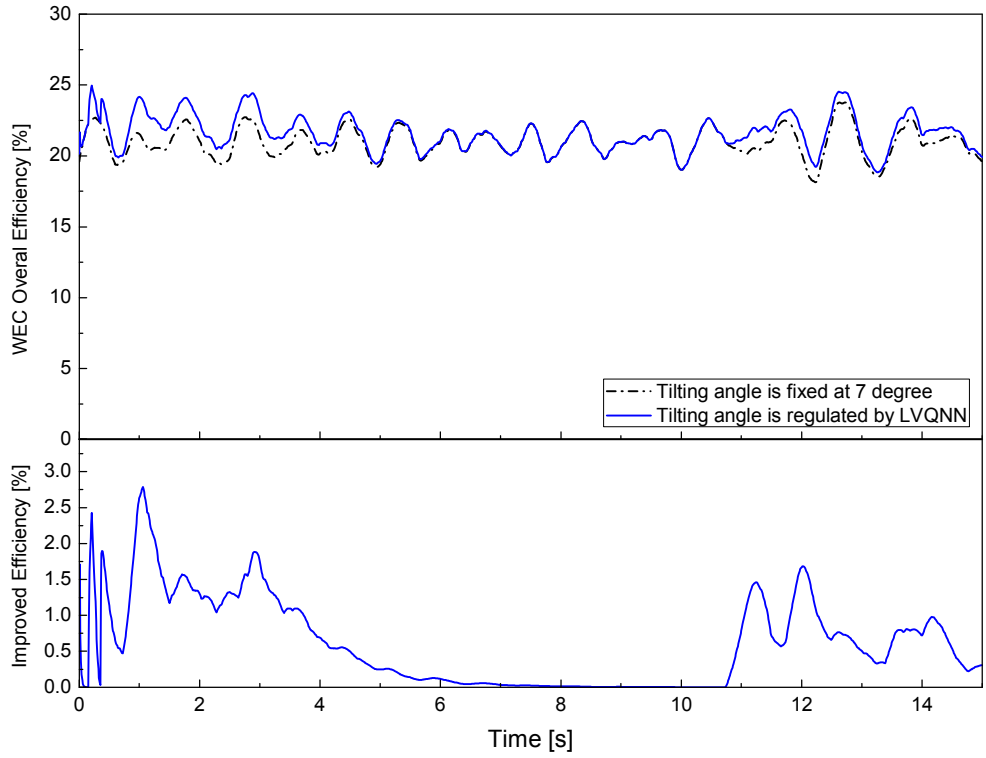


**Fig. 20** Simulation system efficiency comparison in irregular wave condition

## 6. Conclusions

This paper presented a simple approach to maximizing the energy harvesting capability of the LVQNN algorithm based ASAWEC. The supervisor controller, optimized by the training data set, classified wave conditions and generated the desired tilting angle for the secondary controller. At the same time, the PI controller drove the EOM in order to set the ASAWEC at an optimal slope angle. The experimental results with regular waves indicated that by using the proposed control scheme, a decision on the optimal tilting angle could be made within 2s. At these positions, the absorbed energy and energy capture ratio were maximized. In wave case 3, the highest increase in overall efficiency of 5% was achieved compared to the case in which the sliding shaft was fixed in the vertical direction (without changing the tilting angle). In addition, the applicability of the proposed approach in practice was demonstrated by means of simulations of irregular waves.

Use of the LVQNN-based EOM control system does not require system governing equations or information on the transient influence of the waves on the system performance. Therefore, it can be applied to any floating-buoy WEC integrated with an EOM mechanism. Future research works including real-time tests of the controlled system in irregular waves are now being carried out in order to validate the applicability of the proposed method. Then, the suitability of this method for other WEC technologies will be evaluated.

**Acknowledgement**

This work was supported by the New & Renewable Energy of the Korea Institute of Energy Technology Evaluation and Planning (KETEP) grant funded by the Korea government Ministry of Trade, Industry and Energy. (G031518511)

**References**

[1] J. Falnes, A review of wave-energy extraction, Mar. Struct. 20 (4) (2007) 185–201.

[2] J. Falnes, Ocean Waves and oscillating systems, linear interaction including wave-energy Extraction, Cambridge University Press, 2002.

[3] S.H. Salter, J.R.M. Taylor, N.J. Caldwell, Power conversion mechanisms for wave energy, Proc. Inst. Eng. Part M J. Eng. Marit. Environ. 216 (1) (2002) 1-27.

[4] J. Falnes, Optimum control of oscillation of wave-energy converters, Int. J. Offshore and Polar Eng. 12 (2) (2002) 147-155.

[5] R.E. Hoskin, N.K. Nichols, Optimal strategies for phase control of wave energy devices, Utilization of ocean Waves-Wave to Energy Conversion, ASCE, New York, 1987.

[6] M. Kamenský, M. Guglielmi, Optimal control of power take-off from mass spring-damper system, 16th International Conference on Process Control, Slovak Republic, 2007.

[7] A. Babarit, M. Guglielmi, A.H. Clément, Declutching control of a wave energy converter, Ocean. Eng. 36 (2009) 1015–1024.

[8] W. Sheng, R. Alcorn, A. Lewis, On improving wave energy conversion, part II: Development of latching control technologies, Renew. Energy 75 (2015) 935-944.

[9] A.F. Falcão, Phase control through load control of oscillating-body wave energy converters wih hydraulic PTO system, Ocean. Eng. 35 (2008) 58-366.

[10] L. Cuadra, S. Salcedo-Sanz, J.C Nieto-Borge, E. Alexandre, G. Rodríguez, Computational intelligence in wave energy: Comprehensive review and case study, Renew. Sustain. Energy Rev. 58 (2016) 1223–1246.

[11] J. Agrawal, M. Deo, On-line wave predictions, Mar. Struct. 15 (2002) 57-74.

[12] O. Makarynskyy, A. Pires-Silva, D Makarynska, C. Ventura-Soares, Artificial neural networks in wave predictions at the west coast of portugal, Comput. Geosci. 31 (4) (2005) 415-424.

[13] A.A.E Price, T. Mundon, A.F. Murray, A.R Wallace. A test-bed for advanced control of wave energy converters, in 6th European Wave and Tidal Energy Conference, Glasgow, 2005.

[14] D.H. Thinh, D.Q. Truong, N.M. Tri, P.C. Binh, D.T. Dung, S. Lee, H.G. Park, K.K. Ahn, Effects of non-vertical linear motions of a hemispherical-float wave energy converter, Ocean. Eng. 106 (2015) 430-438.

[15] H. Heikkinen, M.J. Lampinen, J. Böling, Analytical study of the interaction between waves and cylindrical wave energy converters oscillating in two modes, Renew. Energy 50 (2013) 50 150-160.

[16] D.Q Truong, K.K. Ahn, Development of a novel point absorber in heave for wave energy conversion, Renew. Energy 65 (2014) 65 183-191.

[17] F.M. White, Fluid Mechanics, McGraw-Hill, 2011.

[18] M.S. Sharif, M. Abbod, A. Amira, H. Zaidi, Artificial Neural Network-statistical approach for PET volume analysis and classification, Adv. Fuzzy Syst. 2012 (2012).

[19] S.C. Ahalt, A.K. Krishnamurthy, P. Chen, D.E. Melton, Competitive learning algorithms for vector quantization, Neural Netw. 3(3) (1990) 277-290.

[20] P. Schneider, M. Biehl, B. Hammer, Adaptive relevance matrices in learning vector quantization, Neural Comput. 21(12) (2009) 3532-3561.

[21] M.E. McComick, Ocean engineering mechanics with applications, Cambridge University Press, UK, 2010.

# APPENDIX

## Table A1

Component selection for the experimented ASAWEC

| Component | Characteristic | Value |
|---|---|---|
| Floating buoy | Diameter | $D_b$ = 1.2m |
| | Height | $H_b$ = 1m |
| | Mass | $m_b$ = 200kg |
| Cylinder | Bore diameter | $D$ = 0.025m |
| | Rod diameter | $d$ = 0.012m |
| | Length of stroke | $L$ = 0.5m |
| Hydraulic motor | Displacement | $D_m$ = 12.5cc/rev |
| Accumulator | Volume | $V_{gas0}$ = 2.8L |
| | Pre-charge pressure | $P_{gas0}$ = 5bar |
| Relief valve | Cracking pressure | $P_{crack}$ = 35bar |
| Hydraulic oil | Effective bulk modulus | 1.5 x$10^9$ [Pa] |
| Flow coefficient | Discharge coefficient | 0.7 |
| MR Rotary brake | Maximum current | 1A |
| | Maximum torque | 5.6Nm |
| | Maximum speed | 1000rpm |
| Linear actuator | Input voltage | 12/24 VDC |
| | Max load capacity | 1600 lbs/ 7000N |
| | Stroke length | 25mm - 600mm |
| | Speed | 6mm/s - 42mm/s |

## Table A2

Water tank and wave maker specifications

| Equipment | Specification | Value |
|---|---|---|
| Water tank | Length | 50m |
| | Width | 20m |
| | Depth | 2m |
| Wave maker | Maximum wave amplitude | 0.5m |
| | Shortest wave period | 0.5s |
| | Cylinder number | 10 |